Free-electron lasing at 27 nanometres based on a laser wakefield accelerator

https://doi.org/10.1038/s41586-021-03678-x

Received: 5 August 2020

Accepted: 28 May 2021

Published online: 21 July 2021

Check for updates

Wentao Wang[1,4]✉, Ke Feng[1,4], Lintong Ke[1,2], Changhai Yu[1], Yi Xu[1], Rong Qi[1], Yu Chen[1], Zhiyong Qin[1], Zhijun Zhang[1], Ming Fang[1], Jiaqi Liu[1], Kangnan Jiang[1,3], Hao Wang[1], Cheng Wang[1], Xiaojun Yang[1], Fenxiang Wu[1], Yuxin Leng[1], Jiansheng Liu[1]✉, Ruxin Li[1,3]✉ & Zhizhan Xu[1]

X-ray free-electron lasers can generate intense and coherent radiation at wavelengths down to the sub-ångström region[1–5], and have become indispensable tools for applications in structural biology and chemistry, among other disciplines[6]. Several X-ray free-electron laser facilities are in operation[2–5]; however, their requirement for large, high-cost, state-of-the-art radio-frequency accelerators has led to great interest in the development of compact and economical accelerators. Laser wakefield accelerators can sustain accelerating gradients more than three orders of magnitude higher than those of radio-frequency accelerators[7–10], and are regarded as an attractive option for driving compact X-ray free-electron lasers[11]. However, the realization of such devices remains a challenge owing to the relatively poor quality of electron beams that are based on a laser wakefield accelerator. Here we present an experimental demonstration of undulator radiation amplification in the exponential-gain regime by using electron beams based on a laser wakefield accelerator. The amplified undulator radiation, which is typically centred at 27 nanometres and has a maximum photon number of around 10^{10} per shot, yields a maximum radiation energy of about 150 nanojoules. In the third of three undulators in the device, the maximum gain of the radiation power is approximately 100-fold, confirming a successful operation in the exponential-gain regime. Our results constitute a proof-of-principle demonstration of free-electron lasing using a laser wakefield accelerator, and pave the way towards the development of compact X-ray free-electron lasers based on this technology with broad applications.

Plasma-based acceleration with ultra-high accelerating gradients (exceeding 100 GV m^{-1}) has attracted increasing interest since it was first proposed[7]. Over the past decade, great progress has been made in the development of laser wakefield accelerators (LWFAs) owing to a series of new techniques for electron injection and guiding[12–19]. LWFAs exploit the immense electrostatic field of the excited plasma wakefield that trails the laser pulse to accelerate particles to high energies over distances of just a few millimetres to several centimetres—thousands of times shorter than those obtained using a conventional radiofrequency accelerator. Quasi-monoenergetic femtosecond electron beams that have peak energies in the GeV range and carry tens of pC of charge have been experimentally generated using LWFAs. LWFAs have considerable potential as an alternative to compact high-energy accelerators. New technologies driven by LWFAs—such as compact X-ray free electron lasers (XFELs)[11], quasi-monoenergetic MeV-class Thomson- and Compton-scattering photon sources[20–22], and even high-energy electron–positron colliders[23]—are being actively pursued globally. In particular, XFELs driven by LWFA-based electron beams are the most promising for X-ray laser sources at a laboratory scale, and they are expected to facilitate various important applications[6].

A free-electron laser (FEL) source consists of an electron accelerator and a periodic magnet array (undulator), which wiggles the high-energy, relativistic electron beam and markedly amplifies the light by means of light–electron interaction as electrons pass through the undulator[1,24]. At X-ray wavelengths, most FEL configurations rely on self-amplified spontaneous emission[2–4], in which the light-amplification process starts from shot noise in the electron beam. Such devices require a stable, high-quality electron beam characterized by six-dimensional brightness, which is defined as the peak current in the electron-beam core divided by the product of the root-mean-square (r.m.s.) transverse normalized emittance and the r.m.s. fractional energy spread in units of 0.1%[17]. However, the robust operation of LWFAs with desirable properties—such as sub-per-cent energy spread and sub-microradian emittance—remains a challenge. Moreover, the transport and focus of such electron beams involves nontrivial complications due to shot-to-shot fluctuations in LWFAs.

[1]State Key Laboratory of High Field Laser Physics and CAS Center for Excellence in Ultra-intense Laser Science, Shanghai Institute of Optics and Fine Mechanics (SIOM), Chinese Academy of Sciences (CAS), Shanghai, People's Republic of China. [2]Center of Materials Science and Optoelectronics Engineering, University of Chinese Academy of Sciences, Beijing, People's Republic of China. [3]School of Physical Science and Technology, ShanghaiTech University, Shanghai, People's Republic of China. [4]These authors contributed equally: Wentao Wang, Ke Feng.
✉e-mail: wwt1980@siom.ac.cn; michaeljs_liu@siom.ac.cn; ruxinli@siom.ac.cn

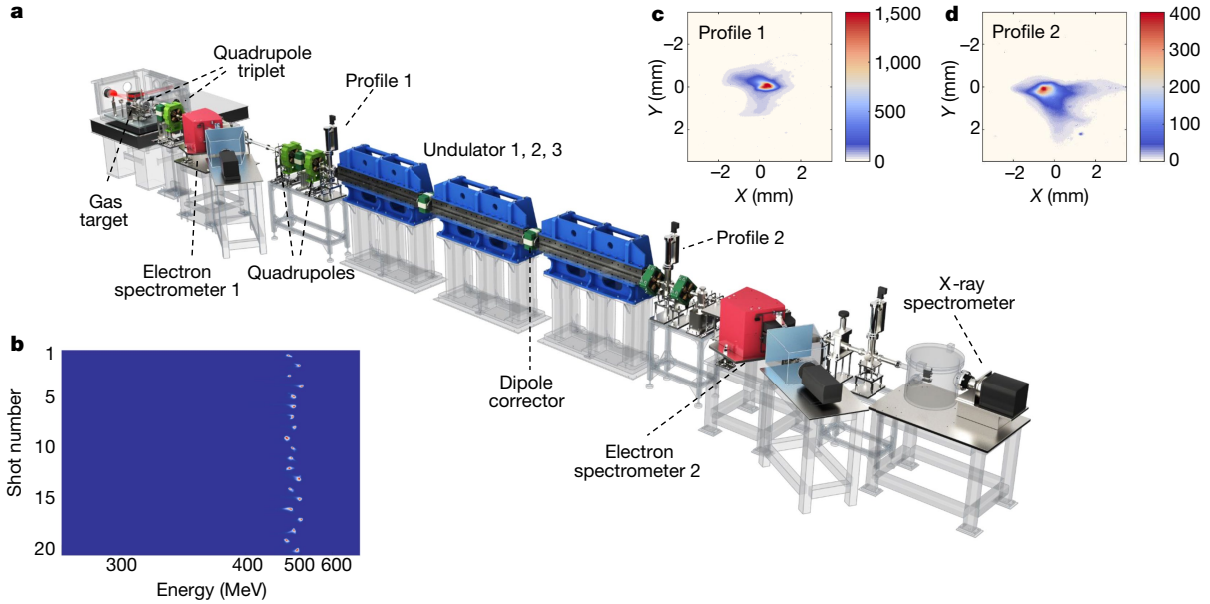

Fig. 1 | Schematic layout of LWFA-based free electron laser experiment. **a**, Undulator beamline with a total length of approximately 12 m from the gas target for the LWFA to the X-ray spectrometer. **b**, Typical spectra of electron beams from the LWFA for 20 consecutive shots. **c**, **d**, Measured transverse profiles of the electron beam at the entrance (**c**) and exit (**d**) of the undulators. The scale bars are normalized.

A qualitative estimation of FEL operation can be obtained from the FEL parameter $\rho = \left[\frac{1}{16}\frac{I_0}{I_A}\frac{K_0^2[JJ]^2}{\gamma_0^3\sigma_\perp^2 k_u^2}\right]^{1/3}$, where I_0 is the beam current, $I_A = 17$ kA is the non-relativistic Alfvén current, γ_0 is the relativistic factor, $\sigma_\perp$ is the r.m.s. transverse size of the beam, $k_u = 2\pi/\lambda_u$ (where λ_u is the undulator period), K_0 is the undulator parameter (for which $[JJ] = [J_0(\xi) - J_1(\xi)]$ for a planar undulator), and J_0 and J_1 are Bessel functions of the first kind[25]. The condition $\sigma_\delta \ll \rho$, where σ_δ is the relative energy spread of the electron beam, is typically required for a high-gain FEL. In state-of-the-art LWFAs, the energy spread of the electron beam is typically of the order of 1% whereas the associated FEL parameter is estimated to be of the order of 0.1%, presenting a substantial obstacle to the realization of a high-gain FEL. Considerable effort has been made to accommodate the requirements of FEL—in particular to handle the initial divergence with permanent magnetic quadrupoles and plasma-based devices[26–28]—and to mitigate the energy spread by using a longitudinal dispersive chicane for beam decompression or a transverse gradient undulator[29,30].

Several projects that have been proposed for the development of an LWFA-based FEL rely on the beam-decompression strategy to mitigate the slice energy spread. The COXINEL collaboration at SOLEIL/Laboratoire d'Optique Appliquée utilizes a chromatic transport scheme to improve the FEL gain and couple the electron beam into a 5-m undulator without strong focusing, in which electrons with various energies are focused at various positions within the undulator[31,32]. The LAOLA collaboration, which involves the University of Hamburg and DESY, developed the concept of the beam-decompression scheme[29,33] and proposed future FEL efforts based on high-gradient quadrupoles and a compact cryo-cooled undulator without strong focusing. The BELLA centre at Lawrence Berkeley National Laboratory used an ultra-high-gradient active plasma lens for beamline shortening and a 4-m-long VISA undulator with strong focusing[28]. Experiments have so far demonstrated the generation of LWFA-based synchrotron undulator radiation in the visible-to-near-infrared regime (500–900 nm) by injecting the electron beam directly into an undulator[34], in the extreme ultraviolet and soft-X-ray region (7–35 nm) by collimating the electron beam with a pair of quadrupoles before it enters an undulator[35], and in the ultraviolet regime (200–300 nm) by decompressing and selecting electrons within a desirable energy range before injection into an undulator[36]. However, these experiments operate in the spontaneous-emission regime without a nonlinear amplification in the undulators.

In this work, we report the generation of undulator radiation with an exponential amplification using an electron beam accelerated by an LWFA. The generated radiation is typically centred at a wavelength of 27 nm and contains a maximum photon number of around 10^{10} per shot, corresponding to a maximum radiation energy of approximately 150 nJ. The extreme-ultraviolet emission intensity as a function of undulator length was measured by disrupting the FEL process with an orbit kick[37], so as to directly verify the exponential amplification. High-brightness electron beams and the fine guiding and transport in the dedicated undulator beamline constitute an unambiguous proof-of-principle demonstration of an FEL using an LWFA.

A schematic of the LWFA-based FEL is shown in Fig. 1a. Experiments were conducted with a 200-TW laser system[38] with a repetition rate of 1–5 Hz. The laser pulses were focused by an off-axis parabolic mirror of *f*-number 32 onto the gas target with a vacuum spot size of 35 μm (full width at half maximum, FWHM) and an energy concentration of around 65% at $1/e^2$. The peak intensity was estimated to be 3.8×10^{18} W cm^{-2}, corresponding to a normalized amplitude of $a_0 = 1.3$. The gas target was manipulated by a perforated baffle inserted upstream of a pure helium supersonic nozzle with diameter of 6 mm. A structured gas flow with a shock front was formed, and contributed to the injection process and to the controllable evolution of the laser pulses. Under the optimized conditions, we obtained high-quality electron beams with a peak energy centred around 490 MeV, an energy spread of around 0.5%, an average integrated charge of around 30 pC and r.m.s. divergence of approximately 0.2 mrad[17] (Fig. 1b). Electron beams were consecutively generated, and the corresponding fluctuations of the electron-beam energy were measured to be less than 3%.

After leaving the plasma, the accelerated electron beam was focused by a group of three quadrupoles—the quadrupole triplet—consisting of a pair of permanent quadrupoles and an electromagnetic quadrupole (Fig. 1a). The permanent magnetic quadrupoles, located 8 cm downstream from the gas target, ensured an effective focusing for handling the initial divergence and reduced the shot-to-shot angular fluctuations of the electron beams. Before entering the undulator, the

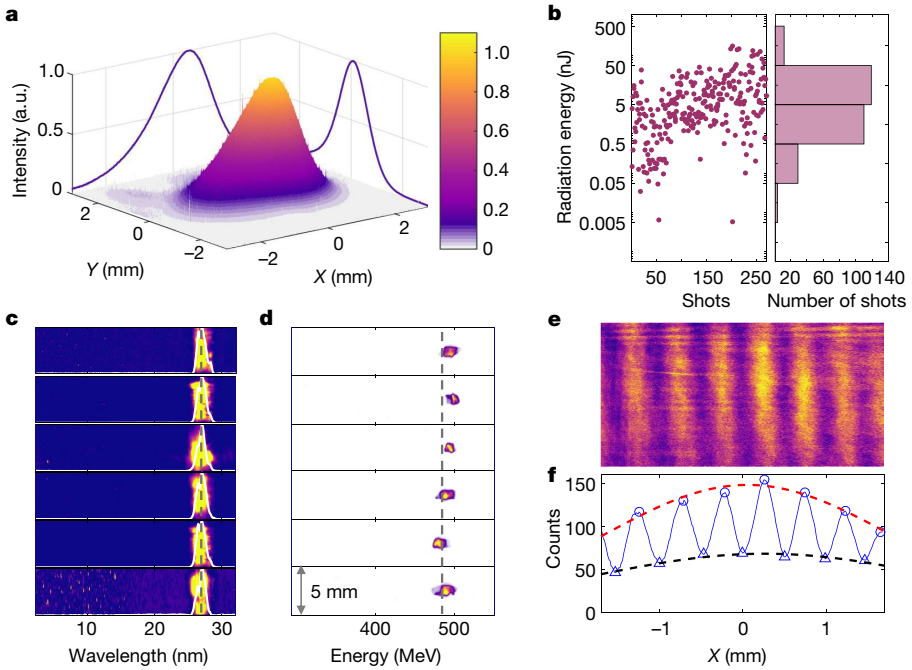

Fig. 2 | Measurement of undulator radiation. a, Measured transverse radiation pattern of a typical pulse on the X-ray CCD camera located 12 m downstream from the gas target. The scale bar is normalized. **b**, Shot-to-shot radiation energy over 270 pulses. **c**, **d**, Measured radiation spectra (**c**) and the corresponding electron-beam energy spectra (**d**) detected by the second spectrometer located at the exit of the undulator. **e**, **f**, Image (**e**) and count profile (**f**) of the interference pattern generated when radiation propagates through two 10-μm slits with a slit separation of 40 μm.

electron beam was adjusted by an additional pair of electromagnetic quadrupoles to retain the minimum transverse sizes throughout the undulator. The parameters of the components in the beamline were optimized for the electron beam with a reference energy of around 490 MeV (see Extended Data Fig. 2). Several beam profile monitors (profiles) equipped with cerium-doped yttrium aluminium garnet (YAG) screens were used at different locations along the beamline to monitor the positions and transverse profiles of the electron beams. With the quadrupoles installed, the measured r.m.s. size of the electron beam was reduced from approximately 0.8 mm to a minimum value of less than 0.1 mm in the horizontal and vertical directions (Fig. 1c). Figure 1d shows the electron-beam profile at the exit of the undulators, and reveals that a relatively small beam size can be maintained in the undulators. The corresponding pointing fluctuations of around 1 mm (r.m.s.) are estimated over 50 shots at the entrance of the undulators (see Extended Data Fig. 4).

When passing through the undulator, the electron beam produced synchrotron undulator radiation with a wavelength centred at the resonant wavelength λ_r, given by $\lambda_r = (1 + K_0^2/2)/2\gamma_0^2$. The interaction between the electrons oscillating in the undulator and the radiation produced led to periodic longitudinal modulation (microbunching) at the period of the resonant wavelength. This result corresponded to a coherent superposition of the radiation. An exponential amplification process developed along the direction of the undulator length. As shown in Fig. 1a, the presented beamline contained three 1.5-m-long undulators with a 10-mm gap and a 25-mm period length, respectively. An associated undulator parameter of $K_0 = 1.41$ was determined, and this yielded an on-axis radiation wavelength of 27.3 nm for the electron beam with a reference energy of 490 MeV. The FEL parameter was therefore estimated as $\rho \approx 5 \times 10^{-3}$ according to the parameters of the obtained electron beams, and the corresponding ideal gain length was $L_{G_0} = \lambda_u/4\pi\sqrt{3}\rho \approx 0.23$ m. The radiation power typically reached saturation after 18–20 gain lengths[24], indicating that a total undulator length of 4.5 m is sufficient for FEL operation in the saturation regime. Considering the degradation that is induced by a non-ideal electron beam, and in particular the large energy spread, the actual gain length would be relatively long. However, the undulator was still sufficiently long for the FEL to operate in the exponential-amplification regime, as illustrated in detail below.

The radiation at the end of the undulators was measured with an X-ray charge-coupled device (CCD) camera (see Methods). Figure 2a shows a typical single-shot transverse profile measurement, which reveals a value of approximately 27 nm. The spot sizes in the horizontal and vertical directions were 2.1 mm and 1.6 mm (FWHM), respectively. The corresponding number of photons collected by the CCD camera was 3.1×10^9, counted within the 3σ range of the radiation signal. Given the transmission of the 0.5-μm-thick Al foil and the quantum efficiency of the CCD camera, the energy of the undulator radiation was calculated to be approximately 30 nJ. The radiation energy distribution over 270 pulses is shown in Fig. 2b. Most of the shots showed a radiation energy of between 0.5 nJ and 50 nJ, and the maximum energy exceeded 150 nJ; this is indicative of operation in the exponential amplification regime, as illustrated below. Figure 2c, d displays the radiation spectra and the corresponding electron-beam spectra over six shots. The centre wavelength of the radiation was 27 nm and the corresponding resonant electron-beam energy was 492.7 MeV; this is in reasonable agreement with the measured average energy of the electron beam (486.2 MeV), considering the 3% variation in the measured peak energy in the second electron spectrometer. Moreover, transverse coherence was deduced from the results of Young's double-slit interference experiment (Fig. 2e, f). An interference fringe visibility of 30% was inferred.

Exponential amplification was verified by introducing a transverse kick of the electron-beam trajectory between two adjacent undulators, at a magnitude sufficient to suppress the amplification process in the downstream undulator. The required critical angle ϕ_c for FEL suppression was determined by $\phi_c = \sqrt{\lambda_r/L_G}$ and was estimated to be 0.35 mrad, where L_G is the power gain length; this could be induced by a pair of x- and y-plane dipole correctors installed between adjacent undulators. In this work, the correctors installed between the second and the third

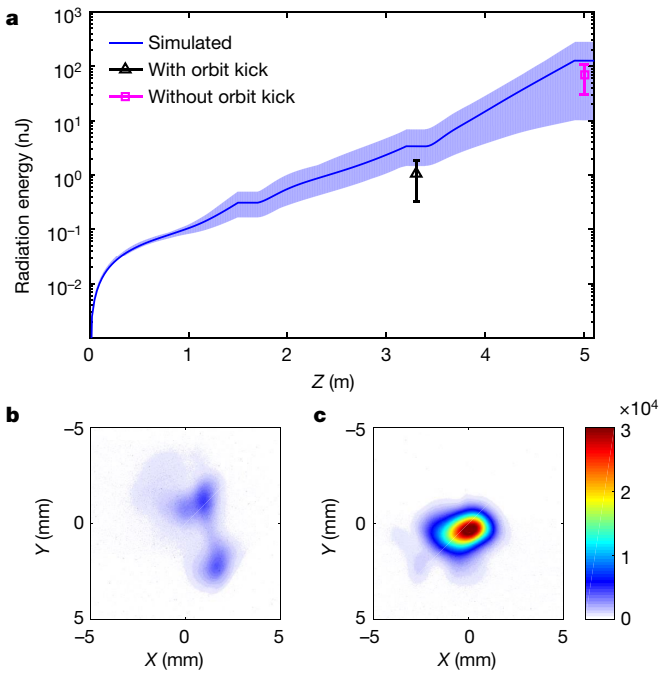

Fig. 3 | Undulator radiation measurement at 27 nm. a, Measured radiation energy with (black) and without (magenta) the orbit kick and the simulated energy along the undulator. Error bars represent the r.m.s. statistical uncertainty in the measured energy averaged over 20 shots. **b**, **c**, Corresponding transverse-beam patterns of the radiation measured with (**b**) and without (**c**) the orbit kick. The scale bar is normalized.

undulators had a maximum magnetic field of 90 Gs. Thus, the maximum deflection angle that could be set for the 500-MeV electron beams is 0.6 mrad. The measured and simulated radiation energy along the undulator and the corresponding measured transverse-beam patterns are presented in Fig. 3a–c. Distorting the trajectory at the beginning of the third undulator could enable the FEL process to restart, leading to secondary spots that are orders of magnitude weaker than those without the orbit kick (Fig. 3b). With the dipole correctors installed, the average measured radiation energy was estimated to be 0.81 nJ with a standard deviation of 0.54 nJ. The radiation energy was measured behind the entire undulator section, which is equivalent to direct measurement at the entrance of the third undulator[37]. The average energy of the radiation without the orbit kick was measured to be 68 nJ, and the maximum obtained gain is approximately 100-fold in the third undulator. These results confirmed successful FEL operation in the exponential-gain regime. In Fig. 3a, only measured radiation energy exceeding 30 nJ (over 20 shots) at the exit of the undulator was included for the evaluation of the average and standard deviation values, which corresponds to the maximum obtained gain and is consistent with the GENESIS simulation[39]. The observed r.m.s. of the fluctuations in relative energy was 54.2%, (Fig. 3a), and the fluctuations show qualitative agreement with those induced by the initial shot noise in the electron beams[40].

As a proof-of-principle demonstration, we have shown the feasibility of LWFA-based FEL at around 27 nm. The high beam quality from the LWFA and the effective guiding of electron beams in the undulator beamline are of crucial importance for the realization of FELs. Our experiments clearly demonstrate exponential amplification of the undulator radiation.

The miniaturization of devices, such as computers and light sources, is highly desirable and has a marked effect on the progress of society. As one of the most advanced light sources, FELs offer the possibility to explore the structures and dynamical processes of atomic and molecular systems at spatial and time resolutions of the order of ångströms and femtoseconds, respectively. As such, they not only bring new innovations to spectroscopy, condensed-matter physics, chemistry, soft matter and structural biology, but also open up new areas of research[6,41]. Compact and low-cost FELs will be essential for expanding their applications and for the further development of transformative technologies. A laboratory-scale, ultra-brilliant FEL (around 10 m in size), with the advantages of low cost (aproximately US$5 million), high temporal resolution (femtosecond-level), high resolution (nanometre-level), and ultra-high precision timing control (less than 1 fs), could gain popularity. However, a lack of reliability and reproducibility of the electron beams is still the main issues that hinders further application of LWFAs. By improving the stability of the driving laser and gas flow, matching the appropriate experimental parameters and developing new injection schemes, it should be possible to repeatedly generate high-quality electron beams and enable further development[42]. In addition, it is necessary to further develop technology with which to analyse femtosecond-duration electron beams from LWFAs, including for detection of the wakefield and for the spatio-temporal structural diagnostics of the electron beam, among other examples. The realization of closed-loop feedback and an automatic optimization system, which are required for further development of LWFAs[42], will enable a table-top FEL to be realized and to gain widespread use.

Online content

Any methods, additional references, Nature Research reporting summaries, source data, extended data, supplementary information, acknowledgements, peer review information; details of author contributions and competing interests; and statements of data and code availability are available at https://doi.org/10.1038/s41586-021-03678-x.

1. Madey, J. M. J. Stimulated emission of bremsstrahlung in a periodic magnetic field. *J. Appl. Phys.* **42**, 1906–1913 (1971).
2. Ackermann, W. et al. Operation of a free-electron laser from the extreme ultraviolet to the water window. *Nat. Photon.* **1**, 336–342 (2007).
3. Emma, P. et al. First lasing and operation of an angstrom-wavelength free-electron laser. *Nat. Photon.* **4**, 641–647 (2010).
4. Ishikawa, T. et al. A compact X-ray free-electron laser emitting in the sub-angstrom region. *Nat. Photon.* **6**, 540–544 (2012).
5. Allaria, E. et al. Highly coherent and stable pulses from the FERMI seeded free-electron laser in the extreme ultraviolet. *Nat. Photon.* **6**, 699–704 (2012).
6. Bostedt, C. et al. Linac Coherent Light Source: the first five years. *Rev. Mod. Phys.* **88**, 015007 (2016).
7. Tajima, T. & Dawson, J. M. Laser electron accelerator. *Phys. Rev. Lett.* **43**, 267–270 (1979).
8. Mangles, S. P. et al. Monoenergetic beams of relativistic electrons from intense laser-plasma interactions. *Nature* **431**, 535–538 (2004).
9. Geddes, C. G. R. et al. High-quality electron beams from a laser wakefield accelerator using plasma-channel guiding. *Nature* **431**, 538–541 (2004).
10. Faure, J. et al. A laser-plasma accelerator producing monoenergetic electron beams. *Nature* **431**, 541–544 (2004).
11. Nakajima, K. Towards a table-top free-electron laser. *Nat. Phys.* **4**, 92–93 (2008).
12. Faure, J. et al. Controlled injection and acceleration of electrons in plasma wakefields by colliding laser pulses. *Nature* **444**, 737–739 (2006).
13. Corde, S. et al. Observation of longitudinal and transverse self-injections in laser-plasma accelerators. *Nat. Commun.* **4**, 1501 (2013).
14. Gonsalves, A. J. et al. Tunable laser plasma accelerator based on longitudinal density tailoring. *Nat. Phys.* **7**, 862–866 (2011).
15. Buck, A. et al. Shock-front injector for high-quality laser-plasma acceleration. *Phys. Rev. Lett.* **110**, 185006 (2013).
16. Liu, J. S. et al. All-optical cascaded laser wakefield accelerator using ionization-induced injection. *Phys. Rev. Lett.* **107**, 035001 (2011).
17. Wang, W. T. et al. High-brightness high-energy electron beams from a laser wakefield accelerator via energy chirp control. *Phys. Rev. Lett.* **117**, 124801 (2016).
18. Steinke, S. et al. Multistage coupling of independent laser-plasma accelerators. *Nature* **530**, 190–193 (2016).
19. Gonsalves, A. J. et al. Petawatt laser guiding and electron beam acceleration to 8 GeV in a laser-heated capillary discharge waveguide. *Phys. Rev. Lett.* **122**, 084801 (2019).
20. Ta Phuoc, K. et al. All-optical Compton gamma-ray source. *Nat. Photon.* **6**, 308–311 (2012).
21. Sarri, G. et al. Ultrahigh brilliance multi-MeV γ-ray beams from nonlinear relativistic Thomson scattering. *Phys. Rev. Lett.* **113**, 224801 (2014).
22. Yu, C. et al. Ultrahigh brilliance quasi-monochromatic MeV γ-rays based on self-synchronized all-optical Compton scattering. *Sci. Rep.* **6**, 29518 (2016).

23. Schroeder, C. B., Esarey, E., Geddes, C. G. R., Benedetti, C. & Leemans, W. P. Physics considerations for laser-plasma linear colliders. *Phys. Rev. Spec. Top. Accel. Beams* **13**, 101301 (2010).
24. Pellegrini, C., Marinelli, A. & Reiche, S. The physics of X-ray free-electron lasers. *Rev. Mod. Phys*. **88**, 015006 (2016).
25. Huang, Z. & Kim, K.-J. Review of X-ray free-electron laser theory. *Phys. Rev. Spec. Top. Accel. Beams* **10**, 034801 (2007).
26. Anania, M. P. et al. An ultrashort pulse ultra-violet radiation undulator source driven by a laser plasma wakefield accelerator. *Appl. Phys. Lett*. **104**, 264102 (2014).
27. Fang, M. et al. Long-distance characterization of high-quality laser-wakefield-accelerated electron beams. *Chin. Opt. Lett*. **16**, 040201 (2018).
28. van Tilborg, J. et al. Active plasma lensing for relativistic laser-plasma-accelerated electron beams. *Phys. Rev. Lett*. **115**, 184802 (2015).
29. Maier, A. R. et al. Demonstration scheme for a laser-plasma-driven free-electron laser. *Phys. Rev. X* **2**, 031019 (2012).
30. Huang, Z., Ding, Y. & Schroeder, C. B. Compact X-ray free-electron laser from a laser-plasma accelerator using a transverse-gradient undulator. *Phys. Rev. Lett*. **109**, 204801 (2012).
31. Loulergue, A. et al. Beam manipulation for compact laser wakefield accelerator based free-electron lasers. *New J. Phys*. **17**, 023028 (2015).
32. Khojoyan, M. et al. Transport studies of LPA electron beam towards the FEL amplification at COXINEL. *Nucl. Instrum. Methods Phys. Res. A* **829**, 260–264 (2016).
33. Seggebrock, T., Maier, A. R., Dornmair, I. & Grüner, F. Bunch decompression for laser-plasma driven free-electron laser demonstration schemes. *Phys. Rev. Spec. Top. Accel. Beams* **16**, 070703 (2013).
34. Schlenvoigt, H. P. et al. A compact synchrotron radiation source driven by a laser-plasma wakefield accelerator. *Nat. Phys*. **4**, 130–133 (2008).
35. Fuchs, M. et al. Laser-driven soft-X-ray undulator source. *Nat. Phys*. **5**, 826–829 (2009).
36. André, T. et al. Control of laser plasma accelerated electrons for light sources. *Nat. Commun*. **9**, 1334 (2018).
37. Ratner, D. et al. FEL gain length and taper measurements at LCLS. In *Proc. 2009 Free-Electron Laser Conference* 221–224 (JACoW, 2009).
38. Wu, F. X. et al. Performance improvement of a 200TW/1Hz Ti:sapphire laser for laser wakefield electron accelerator. *Opt. Laser Technol*. **131**, 106453 (2020).
39. Reiche, S. GENESIS 1.3: a fully 3D time-dependent FEL simulation code, *Nucl. Instrum. Methods Phys. Res. Nucl. Instrum. Methods Phys. Res*. **429**, 243–248 (1999).
40. Hogan, M. et al. Measurements of high gain and intensity fluctuations in a self-amplified, spontaneous-emission free-electron laser. *Phys. Rev. Lett*. **80**, 289–292 (1998).
41. Rossbach, J. et al. 10 years of pioneering X-ray science at the free-electron laser FLASH at DESY. *Phys. Rep*. **808**, 1–74 (2019).
42. Maier, R. et al. Decoding sources of energy variability in a laser-plasma accelerator. *Phys. Rev. X* **10**, 031039 (2020).

Methods

Laser wakefield acceleration

The experiments were conducted with an in-house-developed 200-TW-class laser facility based on chirped pulse amplification[38]. The laser system was optimized with substantial improvements in performance relative to that used in previous experiments in terms of generating a high-brightness electron beam[17]. By optimizing various aspects of the system—such as decreasing the temperature fluctuations of the environmental air conditioning, optimizing the layout of the platform and introducing self-collimating devices—the pointing stability of the laser was optimized from 16 μrad to less than 2 μrad. Moreover, the pulse energy stability improved and reached less than 0.5%. The laser pulses were focused by an off-axis parabolic mirror of *f*-number 32 onto the gas target with a vacuum spot size of 35 μm (FWHM) and an on-target intensity of 3.8×10^{18} W cm^{-2}, yielding a normalized amplitude of $a_0 = 1.3$. The gas target consisted of a perforated baffle inserted upstream of a pure helium supersonic nozzle for constructing a structured gas flow with a shock-front, which contributed to the injection process with a controllable evolution of the driving laser beam. Through the optimization of the back pressure and the distances between the baffle and the gas nozzle, high-quality and stable electron beams were successfully obtained.

Electron beam diagnostic

The accelerated electron beam was deflected by an electron spectrometer (spectrometer 1) located 2.3-m downstream from the gas target, which consisted of a 90-cm-long tunable dipole magnet with a maximum magnetic field of 1.5 T and a Lanex phosphor screen imaged by an intensified charge-coupled device. The measured electron spectrum had a resolution of 0.1% at 500 MeV for the electron beams with 0.1 mrad divergence, and an uncertainty within 12% for the electron beam charge measurement, which was calibrated with an integrating current transformer (Extended Data Fig. 1, Supplementary Video 1). After leaving the undulator, the electron beam was deflected by spectrometer 2 located 10.2-m downstream of the gas target, consisting of the same dipole magnet as the first one. The resulting spectrum showed a high resolution of 0.07% at 500 MeV, and a variation of the measured peak energy of ±3%, caused by the energy fluctuations and pointing instability of the electron beam (Extended Data Fig. 7, Supplementary Videos 2–3).

Electron guiding in the undulator beamline

The accelerated electron beam was focused by a first set of quadrupoles, which consisted of a pair of 5-cm-long permanent magnet quadrupoles with a magnetic field gradient of 250 T m^{-1} and a 10-cm-long electromagnetic quadrupole with a gradient adjustable within the range of 0–80 T m^{-1}. The permanent magnetic quadrupoles were equipped with three-axis motorized translation plates for magnetic axis regulation. The first permanent magnetic quadrupole was located at a fixed position 8 cm downstream of the gas target. The distance between the two permanent quadrupoles was made adjustable to match the beam energy. An additional pair of quadrupoles was applied to ensure the minimum transverse electron beam sizes throughout the three-segment undulators. The positions and transverse profiles of the electron beams were monitored with beam profile monitors equipped with cerium-doped yttrium aluminium garnet screens along the beamline. The total beamline had a length of 12 m from the gas target to the X-ray spectrometer, and the components in the beamline were aligned within ±100 μm of coaxiality with the driving laser beam.

Particle-in-cell simulations

The spectral, quasi-three-dimensional particle-in-cell code FBPIC[43,44] was used to obtain insights into the acceleration stage. The simulation domain has a size of 50 μm and 120 μm in the longitudinal and transverse directions, respectively, with the longitudinal grid size $\Delta z = 31.25$ nm and the transverse grid size $\Delta r = 80$ nm and 16 macroparticles per cell. The laser pulse and density profile were chosen according to the experimental results. A Gaussian laser pulse had a central wavelength $\lambda_L = 0.8$ μm, normalized vector potential $a_0 = 1.3$, waist radius $\omega = 35$ μm and pulse duration $\tau = 25$ fs on FWHM. The density profile used in the simulation was derived from the fringe pattern of the plasma density diagnostic system (Extended Data Fig. 2a). The electrons were injected in the end of the down-ramp region and then rapidly evolved into a positive chirp (the tail of the beam has a higher energy) owing to the positive-slope accelerating field (Extended Data Fig. 2c). As a result of the decrease of a_0 and beam-loading effects, the positive-slope accelerating field became a negative one, and the energy chirp of the electron beam could be compensated (Extended Data Fig. 2d). The energy chirp of the electron beam was compensated sufficiently at the end of the plateau (Extended Data Fig. 2d). The simulated electron beam had a peak energy of 495 MeV, charge of 25.4 pC, global energy spread of 0.67% in r.m.s. (93% of the total electrons), and normalized projected emittance of 0.23 and 0.73 mm mrad in the horizontal and vertical directions, respectively.

Particle tracking

Particle tracking using the Elegant code package[45] up to the second order was performed to investigate the beam performance along the beamline; the results are similar to those of the ASTRA code package[46]. The initial beam used for tracking was obtained from the output of the FBPIC code and the corresponding simulation results are presented in Extended Data Figs. 5, 6.

X-ray diagnostics

The on-axis undulator radiation was detected by an X-ray CCD camera (SOPHIA 2048B, Princeton Instruments) with 2,048 × 2,048 pixels and a pixel size of 15 × 15 μm. The CCD camera was installed under vacuum at the exit of the beamline. A 0.5-μm-thick Al foil was inserted in front of the X-ray CCD to shield it against any residual laser light. The radiation energy was determined from the photons collected by the CCD camera, which was calibrated by a photo-triode (microchannel-plate-based detector). A transmission grating with a groove density of 3,000 lines per mm was installed in front of the X-ray CCD for spectral diagnosis with a highest resolution of 0.1 nm at a wavelength of 30 nm (Extended Data Fig. 8). In addition, the grating was equipped with motorized translation plates to avoid obstruction during measurement of the photon number. The interference fringes were detected when the radiation propagated through two 10-μm slits with a slit separation of 40 μm, placed approxmately 8 cm before a fluorescent Ce:GAGG crystal. An imaging system with a magnification factor of 10 was placed approximately 8 cm after the crystal to improve the resolution.

FEL gain analysis

The FEL power gain length is given by $L_G = L_{G_0}(1 + \Lambda)$, where $\Lambda = a_1\eta_d^{a_2} + a_3\eta_\varepsilon^{a_4} + a_5\eta_\gamma^{a_6} + a_7\eta_\varepsilon^{a_8}\eta_\gamma^{a_9} + a_{10}\eta_d^{a_{11}}\eta_\gamma^{a_{12}} + a_{13}\eta_d^{a_{14}}\eta_\varepsilon^{a_{15}} + a_{16}\eta_d^{a_{17}}\eta_\varepsilon^{a_{18}}\eta_\gamma^{a_{19}}$ quantifies the degrading effects and the three scaled parameters η_d, η_ε and η_γ indicate the diffraction, emittance and energy-spread effects, respectively[47]. With the following parameters: radiation wavelength $\lambda_r = 27$ nm, Twiss parameter $\beta = 5$ m and slice-averaged energy spread $\sigma_\delta = 0.0034$, r.m.s. electron beam size $\sigma_x/\sigma_y = 50/70$ μm on average in the third undulator and peak current $I_p = 5.7$ kA (Extended Data Figs. 3, 5). The scaled parameters take the value $\eta_d = 0.1301$, $\eta_\varepsilon = 0.0138$ and $\eta_\gamma = 0.3623$. Thus, the analysis power gain length in the third undulator can be estimated to be 0.4 m, which shows agreements with the measured value (0.34 m). The exponential amplification was demonstrated by the orbit kick method (Fig. 3) and was also verified by comparing the lasing and not lasing conditions (Extended Data Fig. 9).

Data availability

All data are available upon reasonable request from the corresponding authors. Source data are provided with this paper.

Code availability

All codes written for use in this study are available upon reasonable request from the corresponding authors.

43. Lehe, R. et al. A spectral, quasi-cylindrical and dispersion-free Particle-In-Cell algorithm. *Comput. Phys. Commun.* **203**, 66 (2016).
44. Jalas, S. et al. Accurate modeling of plasma acceleration with arbitrary order pseudo-spectral particle-in-cell methods. *Phys. Plasmas* **24**, 033115 (2017).
45. Borland, M. *ELEGANT: A flexible SDDS-compliant code for accelerator simulation*. Technical Report No. LS-287 (Argonne National Laboratory, 2000).
46. Flöttmann, K. ASTRA. A space charge tracking algorithm. https://www.desy.de/~mpyflo/ (DESY, 2007).
47. Xie, M. Exact and variational solutions of 3D eigenmodes in high gain FELs. *Nucl. Instrum. Methods Phys. Res. Sect. A* **445**, 59–66 (2000).

Acknowledgements We thank D. Wang and B. Liu for discussions and assistance. This work was supported by the Strategic Priority Research Program (B) (grant no. XDB16) and Center for Excellence in Ultra-intense Laser Science of Chinese Academy of Sciences (CAS), the National Natural Science Foundation of China (grant nos. 11127901, 11875065 and 11991072), the Natural Science Foundation of Shanghai (nos 18JC1414800 and 18ZR1444500) and the State Key Laboratory Program of the Chinese Ministry of Science and Technology and CAS Youth Innovation Promotion Association (Y201952).

Author contributions R.L., Jiansheng Liu and Z.X. conceived the project. R.L., W.W. and K.F. designed the experiments. W.W., K.F., L.K., C.Y., R.Q., Y.C., Z.Q., Z.Z., M.F., Jiaqi Liu, K.J., H.W., C.W. and Jiansheng Liu performed the experiments and collected the data. Y.L., Y.X., F.W. and X.Y. constructed and ran the Ti:sapphire laser system. K.F. conducted the simulations. K.F. and L.K. analysed the experimental data. K.F., W.W. and R.L. co-wrote the paper. All authors contributed to the experiments and discussions.

Competing interests The authors declare no competing interests.

Additional information

Supplementary information The online version contains supplementary material available at https://doi.org/10.1038/s41586-021-03678-x.

Correspondence and requests for materials should be addressed to W.W., J.L. or R.L.

Peer review information *Nature* thanks Luca Giannessi, James Rosenzweig and the other, anonymous, reviewer(s) for their contribution to the peer review of this work. Peer reviewer reports are available.

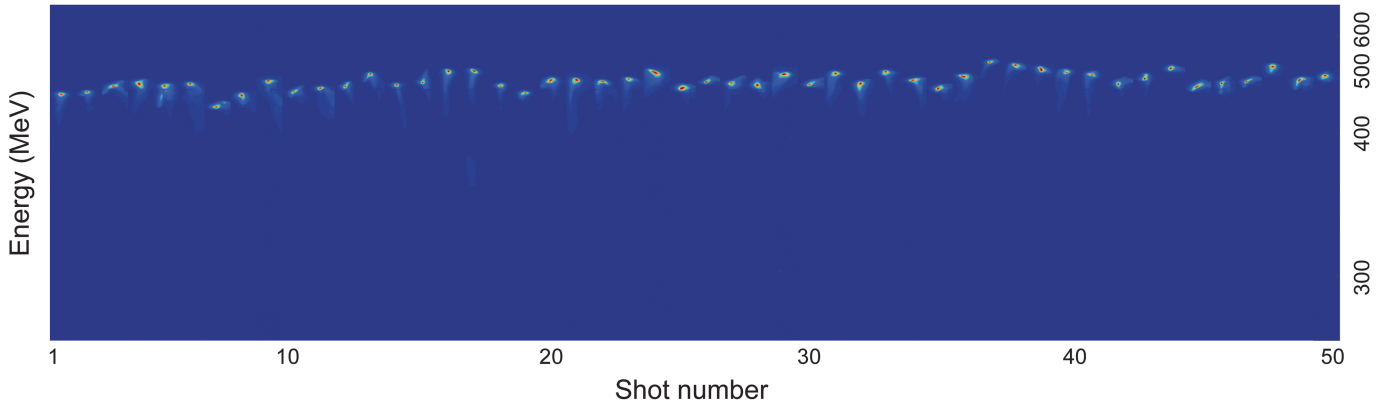

Extended Data Fig. 1 | Electron-beam spectra from LWFA. Energy spectra of the accelerated electron beams for 50 shots measured in spectrometer 1 located 2.3-m downstream of the gas target. Electron beams with an average peak energy of about 490 MeV, r.m.s. energy spread of 0.2–1.2%, r.m.s. divergence of 0.1–0.4 mrad and charges of 10–50 pC were experimentally obtained. The associated fluctuations of the electron beam peak energy were estimated to be less than 3%.

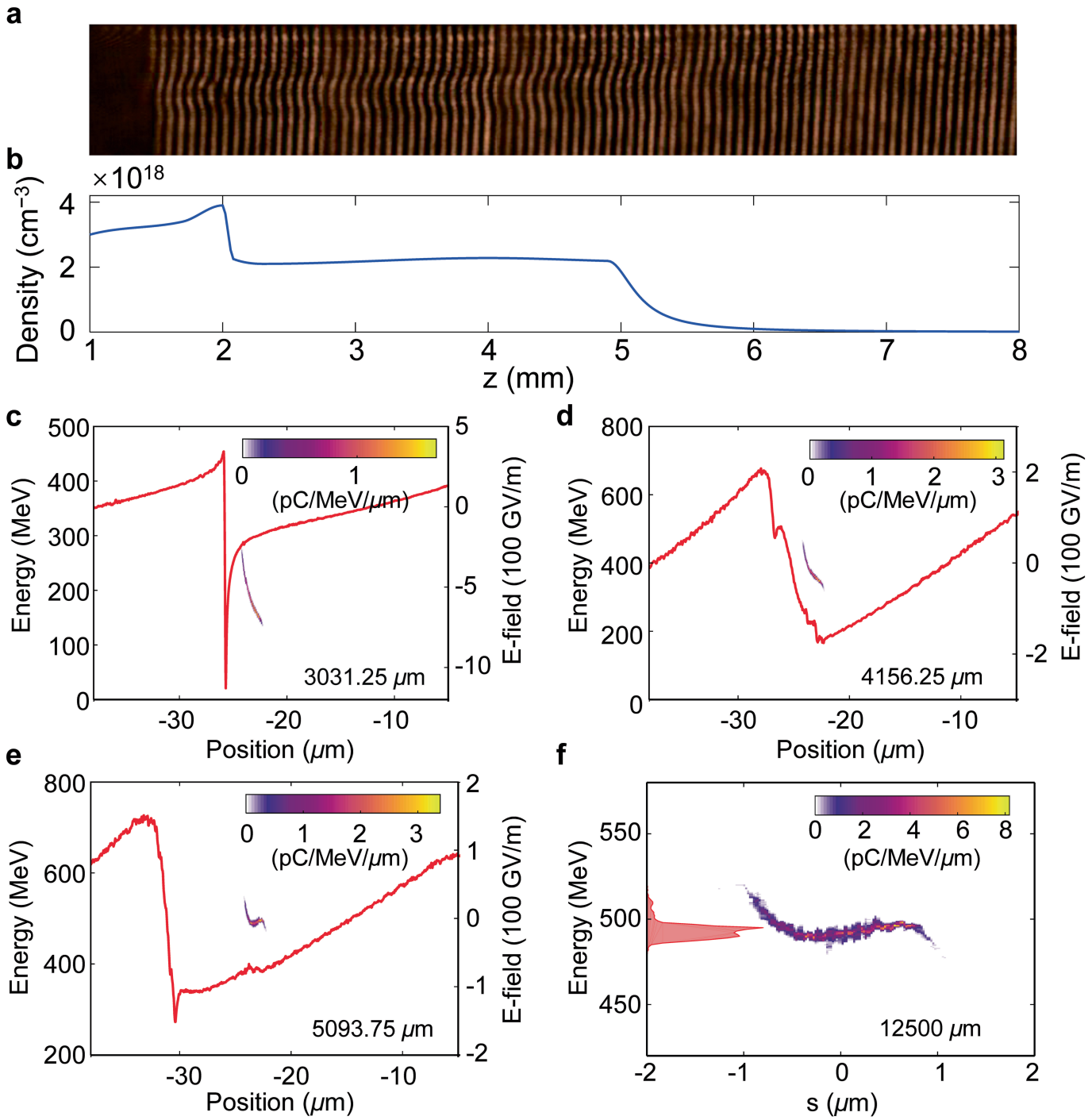

Extended Data Fig. 2 | Particle-in-cell simulation results for single-stage LWFA. a, **b**, Measured fringe pattern for plasma density diagnosis and the corresponding density profile along the optical axis. **c**–**e**, Longitudinal phase space of the trapped electrons and the corresponding accelerating electric field at different positions. **f**, Longitudinal phase space of the accelerated electrons at the exit of the plasma and the corresponding energy spectrum shown in red. *s* is the longitudinal position of the electron in an electron beam in the co-moving coordinate. The simulated electron beam had a peak energy of 495 MeV, charge of 25.4 pC, global energy spread of 0.67% in r.m.s. (93% of the total electrons), and normalized projected emittance of 0.23 mm mrad and 0.73 mm mrad in the horizontal and vertical directions, respectively.

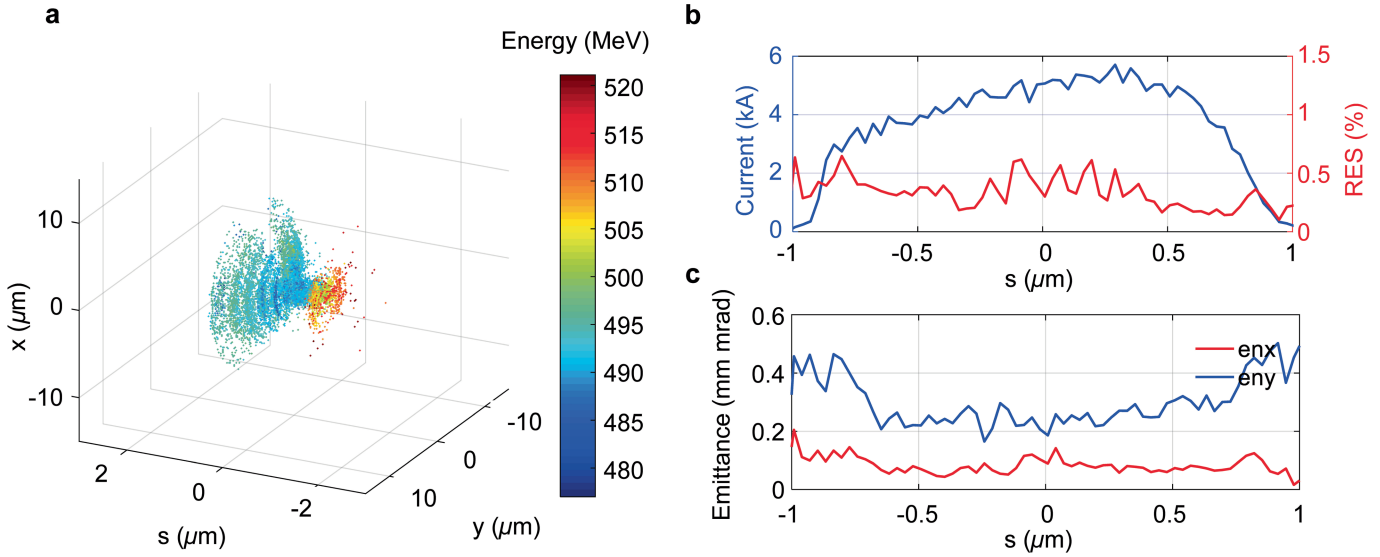

Extended Data Fig. 3 | Properties of simulated electron beam at the exit of the plasma. a, Coordinate space distribution of accelerated electrons, with various colours representing the various energies. **b**, Beam current (blue) and slice energy spread (red) within the beam. RES, relative energy spread. **c**, Normalized slice emittance of the beam in the horizontal (enx, red) and vertical (eny, blue) directions. Each slice has a length of 31.25 nm, which was set as the grid size in the particle-in-cell simulation.

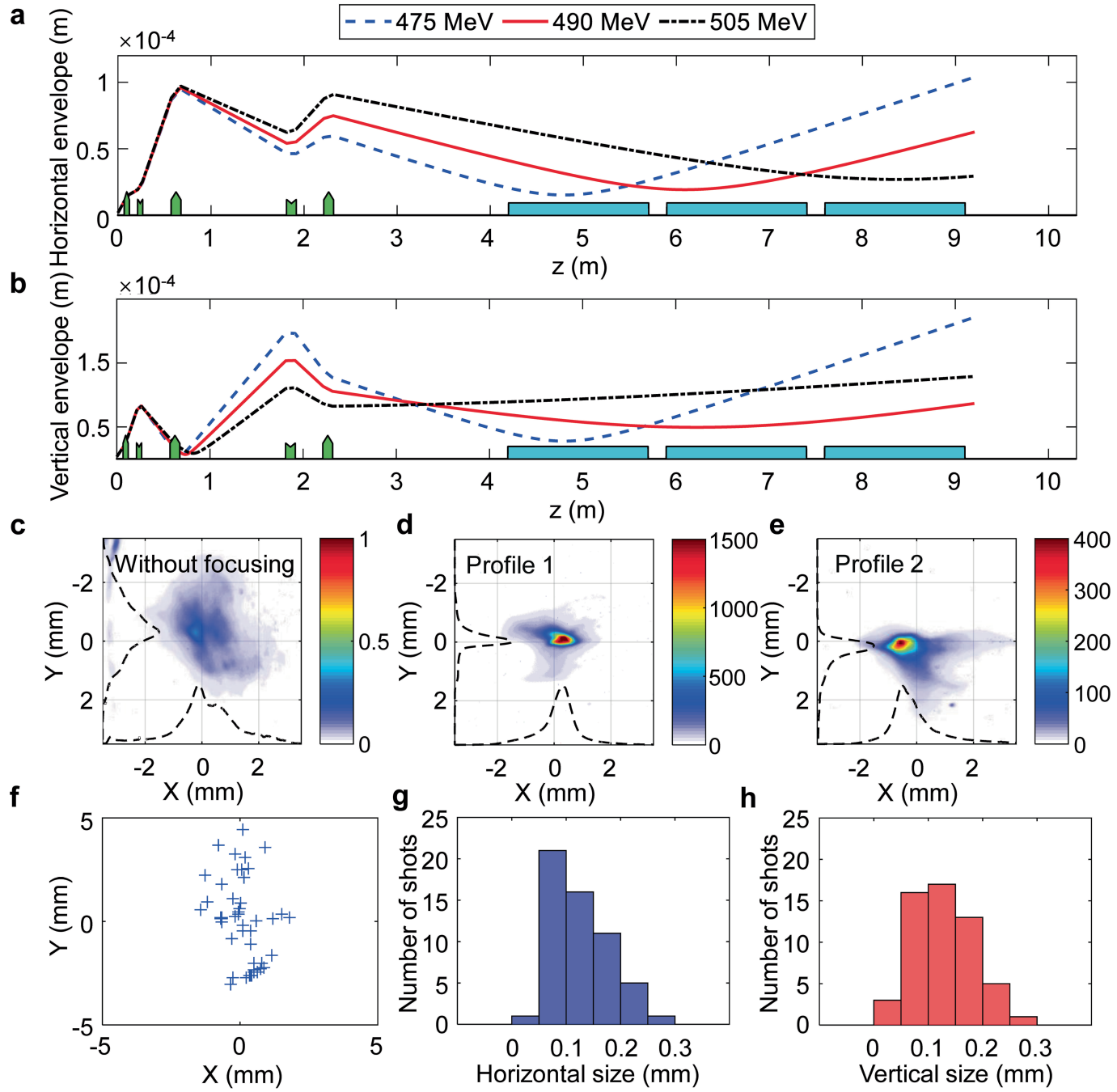

Extended Data Fig. 4 | Electron-beam properties in the beamline. **a**, **b**, Start-to-end simulation for horizontal and vertical envelopes of the electron beam along the beamline with a beam energy of 475 MeV (blue), 490 MeV (red) and 505 MeV (black). **c**–**e**, Measured transverse profiles of the electron beam at the entrance of the undulator located 4-m downstream from the gas target without (**c**) and with (**d**) focusing and at the exit of the undulator located 9.5-m downstream from the gas target (**e**). With the quadrupoles installed, the measured r.m.s. size of the electron beam was reduced from approximately 0.8 mm to a minimum value of less than 0.1 mm in the horizontal and vertical directions. **f**–**h**, Shot-to-shot pointing distribution over 50 shots (**f**), and beam size statistics in the horizontal (**g**) and vertical (**h**) directions. The relative positions of the quadrupoles (green) and undulators (cyan) are shown in **a** and **b**.

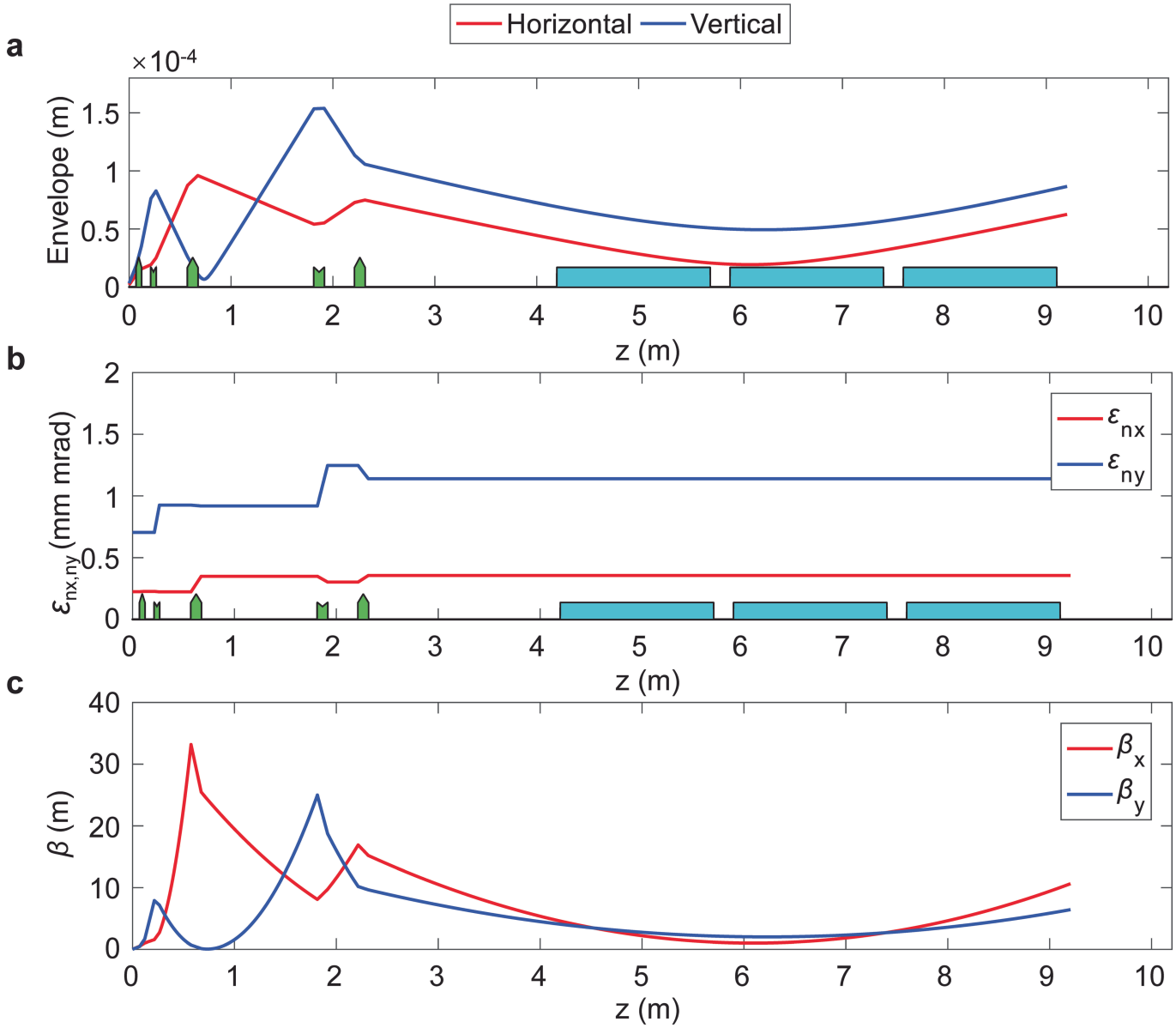

Extended Data Fig. 5 | Properties of an electron beam with a reference energy of 490 MeV along the beamline. a–**c**, Simulated beam envelopes (**a**), normalized projected emittance (**b**) and Twiss parameters β (**c**) of the electron beam in the horizontal (red) and vertical (blue) directions. The beam used for tracking was directly derived from the FBPIC code.

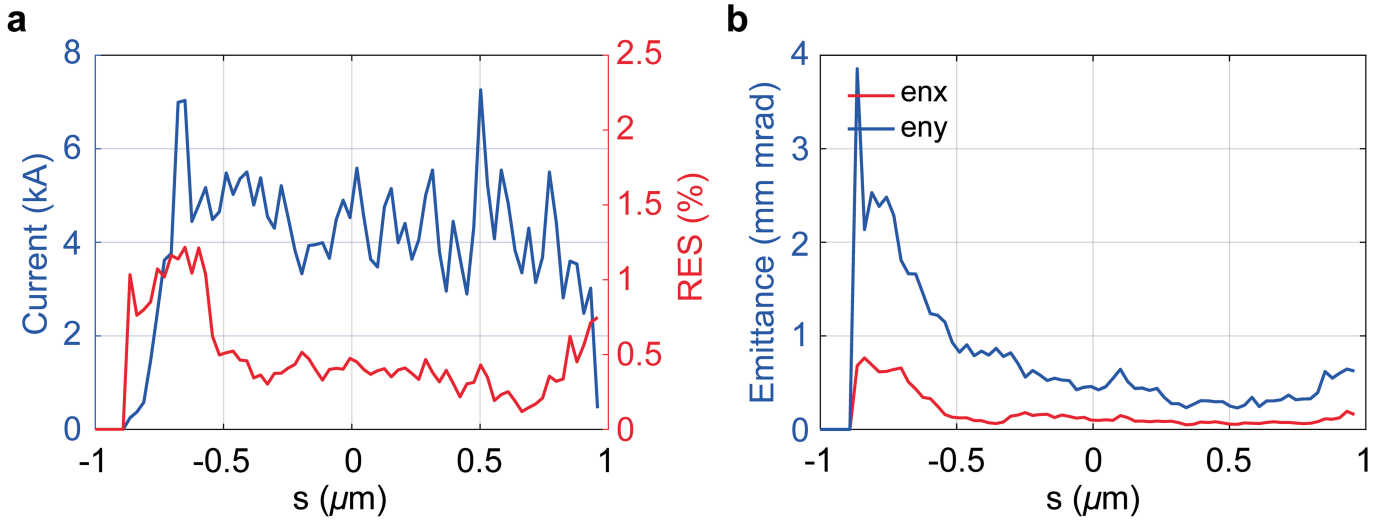

Extended Data Fig. 6 | Properties of the electron beam at the entrance of the undulator. a, Beam current (blue) and slice energy spread (red) within the beam. **b**, Normalized slice emittance of the beam in the horizontal (red) and the vertical (blue) directions. Despite the slice emittance in the bunch tail increasing substantially (**b**) and causing an increase in projected emittance (Extended Data Fig. 5b), most of the electrons in the beam still showed a small slice emittance.

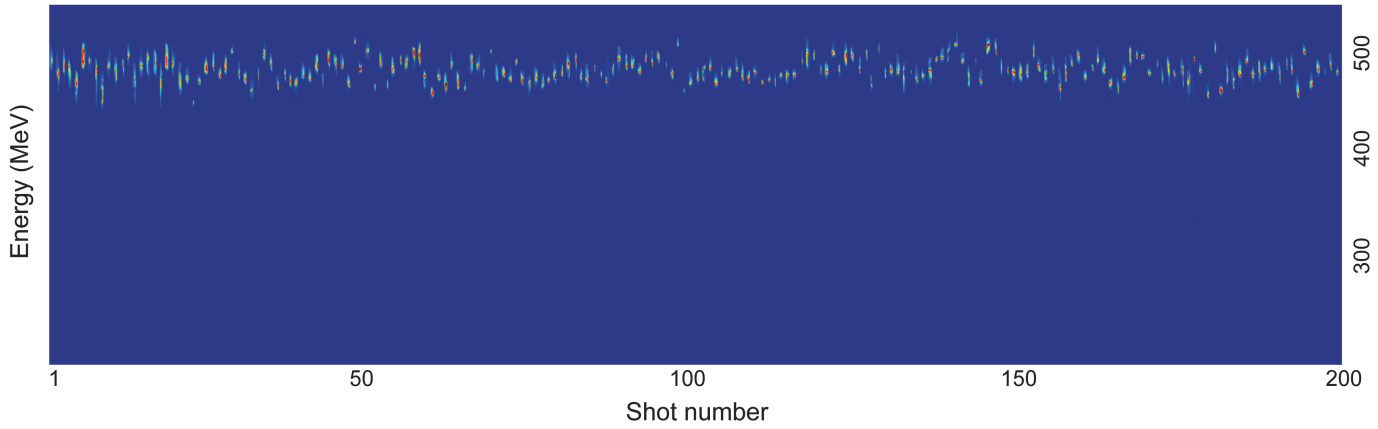

Extended Data Fig. 7 | Electron-beam spectra detected at the exit of the undulators. Energy spectra of electron beams for 200 consecutive shots detected with spectrometer 2. The average energy of the electron beam was estimated to be 485 MeV with energy fluctuations of 3.3% and a reproducibility of approximately 100%.

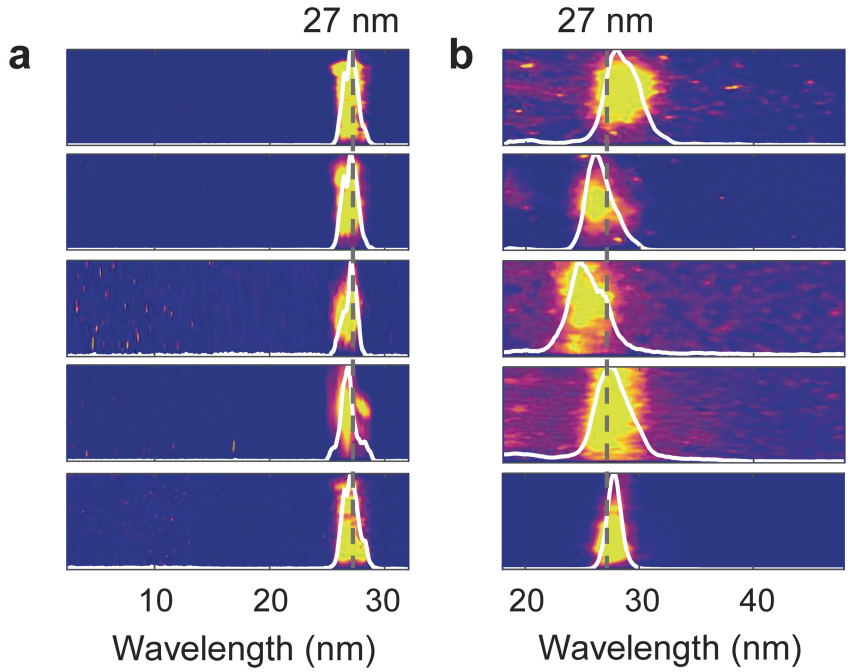

Extended Data Fig. 8 | Measured spectra of undulator radiation. **a**, **b**, Spectra of the undulator radiation with a groove density of the grating of 3,000 lines per mm (**a**) and 500 lines per mm (**b**). The radiation wavelength was typically centred at 27 nm with a corresponding electron beam energy of 492 MeV, which is reasonably consistent with the measured values shown in Extended Data Fig. 7. The minimum bandwidth was measured to be 2%, which indicated a reasonable agreement with the simulated values in the exponential-gain regime. The measured spectra of broadband spontaneous emission are also depicted with a bandwidth of approximately 7%.

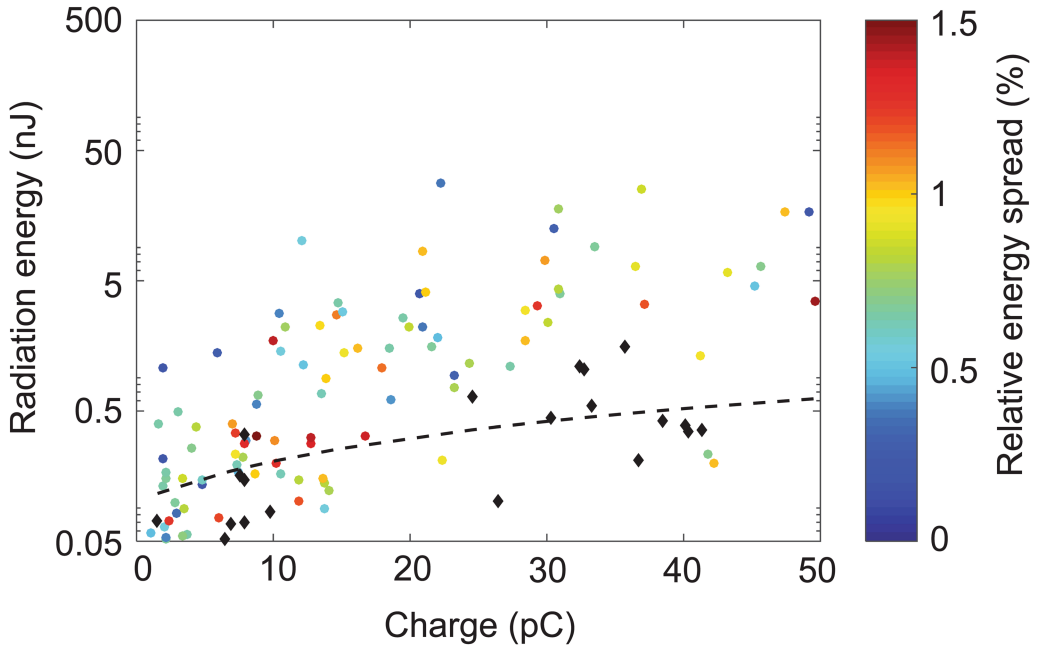

Extended Data Fig. 9 | Measured radiation energy at the exit of the undulator for various electron beam charges and relative energy spreads. The black diamonds represent cases with energy spreads larger than 2% (exponential gain is typically not available under such conditions), and the corresponding linear fitting curve (black dashed line) indicates the spontaneous emission. The radiation emitted by a low-energy-spread electron beam (<1%) typically has energy one to two orders higher than that in spontaneous cases, thus indicating the operation in the exponential-gain regime in the present scheme. The exponential gain of the radiation is illustrated with the orbit kick method in the main text.